



Contents lists available at ScienceDirect

## Journal of Quantitative Spectroscopy &amp; Radiative Transfer

journal homepage: [www.elsevier.com/locate/jqsrt](http://www.elsevier.com/locate/jqsrt)

# Characterizing the size and absorption of single nonspherical aerosol particles from angularly-resolved elastic light scattering



Sequoyah Walters<sup>a</sup>, Jason Zallie<sup>a</sup>, Gabriel Seymour<sup>a</sup>, Yong-Le Pan<sup>b</sup>, Gorden Videen<sup>b</sup>, Kevin B. Aptowicz<sup>a,\*</sup>

<sup>a</sup> Department of Physics, West Chester University, West Chester, PA 19383, USA

<sup>b</sup> US Army Research Laboratory, 2800 Powder Mill Road, Adelphi, MD 20783, USA

## ARTICLE INFO

## Article history:

Received 18 September 2018

Revised 3 December 2018

Accepted 3 December 2018

Available online 4 December 2018

## Keywords:

Single particle

Absorption

Elastic light scattering

Aerosol

## ABSTRACT

Measuring the absorption of a single aerosol particle is a challenging endeavor. Of the few techniques available, none are suitable for measuring the single-particle absorption of coarse-mode nonspherical aerosols. Analysis of two-dimensional angular optical scattering (TAOS) patterns provide a possible pathway to perform this measurement. Using a Multiple-Sphere T-Matrix (MSTM) code, we simulate the captured TAOS patterns with geometries similar to a previously designed instrument. By analyzing the size of the speckle and the integrated irradiance of these simulated TAOS patterns, we are able to distinguish between high-absorbing, weak-absorbing, and non-absorbing particles over the size range of 2  $\mu\text{m}$  to 10  $\mu\text{m}$ . In particular, the speckle present in the scattering patterns provides a means to estimate the size of the particle. Once the size of the particle is known, the integrated irradiance provides insight into the absorption of the particle.

© 2018 Elsevier Ltd. All rights reserved.

## 1. Introduction

Our atmosphere is composed of absorbing aerosol particles ranging from high-absorbing black carbon to less-absorbing mineral dust and brown carbon [1–3]. Absorbing aerosol particles affect our Earth's climate as well as pose a risk to public health [4–7]. As such, monitoring and characterizing the regional and global distribution of these aerosol particulates is of great interest.

Measuring the temporal and spatial distribution of absorbing aerosol particles in our atmosphere requires a multifaceted approach. Although remote sensing using ground stations and satellites is needed for adequate spatial and temporal coverage, in situ measurements in aircraft and at surface stations serve to constrain, improve, and test inversion algorithms [5]. Furthermore, single-particle measurements of absorption provide critical insights that would be lost when performing ensemble measurements [8,9].

A number of techniques have been described in the literature to measure the absorptive properties of single aerosol particles. Willoughby et al. describe a method in which a particle is heated with laser light and the imaginary component of refractive index is determined by monitoring the angular variation of elastically scattered light [10]. However the analysis is limited to spherical parti-

cles. Nakagawa et al. designed a single-particle polar nephelometer that determines the complex refractive index of droplets of an aqueous solution of nigrosine dye by comparing the angular scattering with Mie theory [11]. Again, the analysis of the complex refractive index is limited to spherical particles. Gong et al. utilize an optical trap in combination with cavity ringdown spectroscopy to measure the extinction of light from both spherical and nonspherical single aerosol particles, but the analysis does not delineate between the contributions of absorption and scattering to extinction [12].

An instrument more widely used in field campaigns is the Single Particle Soot Photometer (SP2) [13,14]. It measures the refractory black carbon mass of individual black carbon particles by laser-induced incandescence [15–17]. The particle size range for this measurement is approximately 70 to 500 nm mass equivalent diameter, although it depends upon particle density. In addition to measuring the refractory black carbon mass, the SP2 estimates the particle size by measuring an elastic scattering signal. Moteki et al. used the elastic scattering signal of the SP2 as well as the mass determined from an aerosol particle mass analyzer (APM) to estimate the refractive indices of small nonspherical particles [18]. In particular, when invoking the Raleigh–Gans approximation, the scattering cross-section of small aerosol particles is primarily a function of the complex refractive index and particle volume. The particle volume can be estimated by measuring the mass with an APM and assuming a density. The scattering cross-section can be esti-

\* Corresponding author.

E-mail address: [kaptowicz@wcupa.edu](mailto:kaptowicz@wcupa.edu) (K.B. Aptowicz).

mated from the elastic light scattering signal detected by the SP2. Using these two measurements and an assumed relationship between the real and imaginary parts of the refractive index, Moteki et al. determine the complex refractive index of ambient soot sampled in Tokyo, Japan. Although it is not clear how stringently the criteria of the Rayleigh-Gans approximation needs to be met, it appears the particle needs to be less than 300 nm in diameter for the analysis to be successful.

In this work, we present an approach for characterizing the absorption of single, non-spherical particles in the coarse-mode size range. This is an inaccessible parameter space using the techniques discussed above. Using a publicly available MSTM code [19], we calculate two-dimensional angular optical scattering (TAOS) patterns. The calculated TAOS patterns are meant to simulate TAOS patterns that can be captured by a previously described instrument [9]. We show that the size of the sphere clusters can be estimated by analyzing the size of the speckle in the simulated TAOS patterns. In addition, we explore how the integrated irradiance of the TAOS patterns, which correlates with the scattering cross-section, depends upon complex refractive index. Using the speckle-based measurement of particle size and approximate scattering cross-section from the integrated irradiance, we are able to distinguish between particles with various refractive indices from highly absorbing to non-absorbing over a size range of 2  $\mu\text{m}$  to 10  $\mu\text{m}$ . We conclude by discussing the limitations of our approach and the next steps for further validating the technique.

## 2. Background

The intensity and angular distribution of light scattered from an aerosol particle depend upon particle size, shape, and composition. For example, it is well known that the scattering cross-section of a particle (i.e. the ratio between the radiant energy flux of light scattered by the particle and the incident irradiance) generally increases with particle size. Indeed, many particle sizing instruments are based on this property, such as products from ClimeT Instruments Company, Droplet Measurement Technologies, and TSI Incorporated. However, single-particle absorption can also affect the scattering cross-section [18,20]. Thus, in addition to size, the scattering cross-section of an aerosol particle contains information about the absorptive properties.

A simple simulation conveys this dependence of the scattering cross-section on both particle size and absorption. Details about the simulation can be found in Section 3. Fig. 1(a) shows the backward- and forward-scattering hemispheres of a cluster of tightly-packed spheres where the nominal diameter of the cluster is 8  $\mu\text{m}$  and the wavelength of the incident light is 532 nm. The complex refractive index of the constituent spheres in the cluster is  $1.53 + i0$ . By shrinking the cluster to a size of 5.6  $\mu\text{m}$ , the scattering cross-section decreases by a factor of two. The scattering hemispheres of this small non-absorbing cluster are shown in Fig. 1(b). However, the same reduction in scattering cross-section can occur by changing the absorption of the particle rather than the cluster size. This can be done by keeping the diameter of the cluster at 8  $\mu\text{m}$  but increasing the imaginary part of the refractive index of the constituent spheres from 0 to 0.1. The scattering hemispheres of this large, highly-absorbing cluster are shown in Fig. 1(c). This simple example displays a central idea in this paper. In particular, if the size of the particle is accounted for, insight into single-particle absorption can be discerned from elastic light scattering.

This example illustrates another central idea of this work. Looking closely at the scattering patterns in Fig. 1, the speckle in the scattering hemispheres increases in size and decreases in number as the cluster size shrinks from 8  $\mu\text{m}$  to 5.6  $\mu\text{m}$ . Multiple groups have noted and studied this effect [21–27]. For example, Ulanowski et al. explore the correlation between the average inverse area of

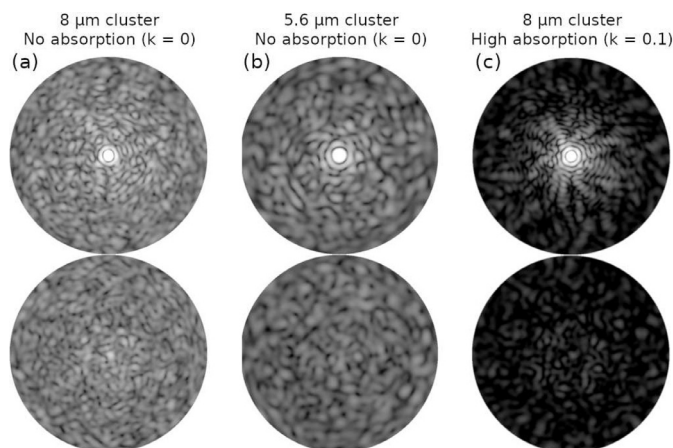


**Fig. 1.** Simulated angular-resolved light scattering from sphere clusters. Each cluster is composed of 84 constituent spheres. Forward-scattering hemispheres (top row) and backward-scattering hemispheres (bottom row) are shown for (a) an 8  $\mu\text{m}$  cluster of spheres with no absorption ( $k = 0.0$ ), (b) a 5.6  $\mu\text{m}$  small cluster of spheres with no absorption, and (c) an 8  $\mu\text{m}$  cluster of spheres with high absorption ( $k = 0.1$ ). To emphasize the features, a logarithmic scale is used for the brightness.

the speckle and the aerosol nominal size [23]. Holler et al. show a correlation between the mean number of local peaks and valleys in intensity in the scattering pattern and the diameter of a cluster of spheres [21]. Brunel et al. estimate the dimensions of a particle by analyzing the central peak of the 2D-autocorrelation of the speckle pattern [26]. Thus the size of the particle, which affects the scattering cross-section, can be estimated from analysis of the speckle. By accounting for particle size by analyzing the speckle, the scattering cross-section can provide insight into the absorption of micron-sized nonspherical particles.

To further refine these ideas, we simulate the light-scattering patterns (i.e. TAOS patterns) collected by a previously realized instrument [9]. Fig. 2(a) shows a simplified diagram of the light-scattering collection optics. More details about the instrument are provided in previous published papers [9,28]. By using an ellipsoidal mirror, a very large solid angle of scattered light can be detected spanning the polar scattering angle from  $12^\circ$  to  $168^\circ$  and the azimuthal scattering angle from  $0^\circ$  to  $360^\circ$ , although the experimental geometry significantly reduces the azimuthal coverage for certain polar angles. Fig. 2(b) depicts the captured TAOS pattern from a spherical particle. The polar and azimuthal scattering angles mapped onto the detector plane are shown in Fig. 2(c) and (d). The direction of the incident laser beam determines  $0^\circ$  for the polar scattering angle. The  $0^\circ$  for the azimuthal scattering angle is arbitrarily chosen. The dark black regions in the TAOS pattern are scattering angles not captured due to the instrument geometry. The forward- and backward-scattering hemispheres are estimated from the raw TAOS pattern by identifying the polar and azimuthal scattering angles associated with each pixel of the TAOS pattern and interpolating the irradiance of the forward- and backward-scattering hemispheres. The scattering hemispheres for 2 atmospheric nonspherical particles are shown in Fig. 3. Again, the dark black regions are scattering angles inaccessible by the experimental geometry. The scattering patterns from both particles have similar speckle size, suggesting the particles are of similar size. However, the integrated irradiance (i.e. the sum of the photoelectron counts of all the pixels) of Fig. 3(a) is six times larger than Fig. 3(b). A possible interpretation of these findings is the particle that created the scattering pattern shown in Fig. 3(b) was much more absorptive than the particle that created the scattering pattern shown in Fig. 3(a). We commonly find similar examples in

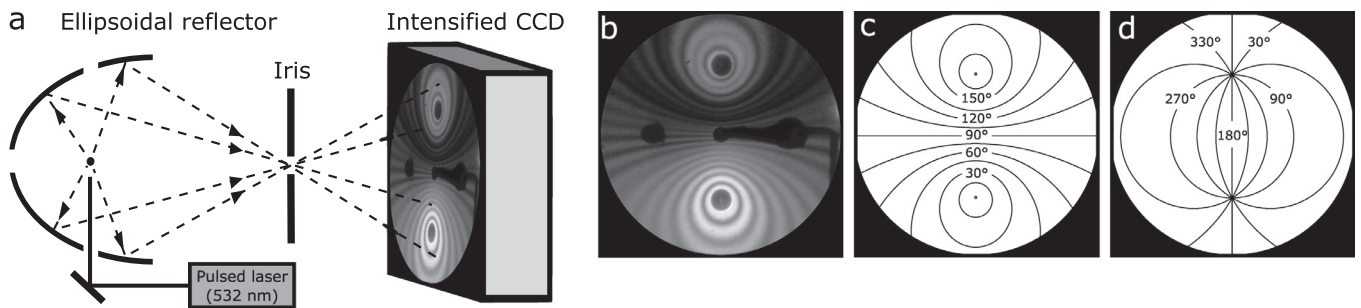


**Fig. 2.** (a) Schematic of an apparatus that has been used to measure TAOS patterns [9]. The design allows for simultaneous measurement of the forward- and backward-scattering hemispheres from single aerosol particles. (b) A sample TAOS pattern measured from a spherical particle. (c) Polar coordinates mapped onto the detector plane. (d) Azimuthal coordinates mapped onto the detector plane.

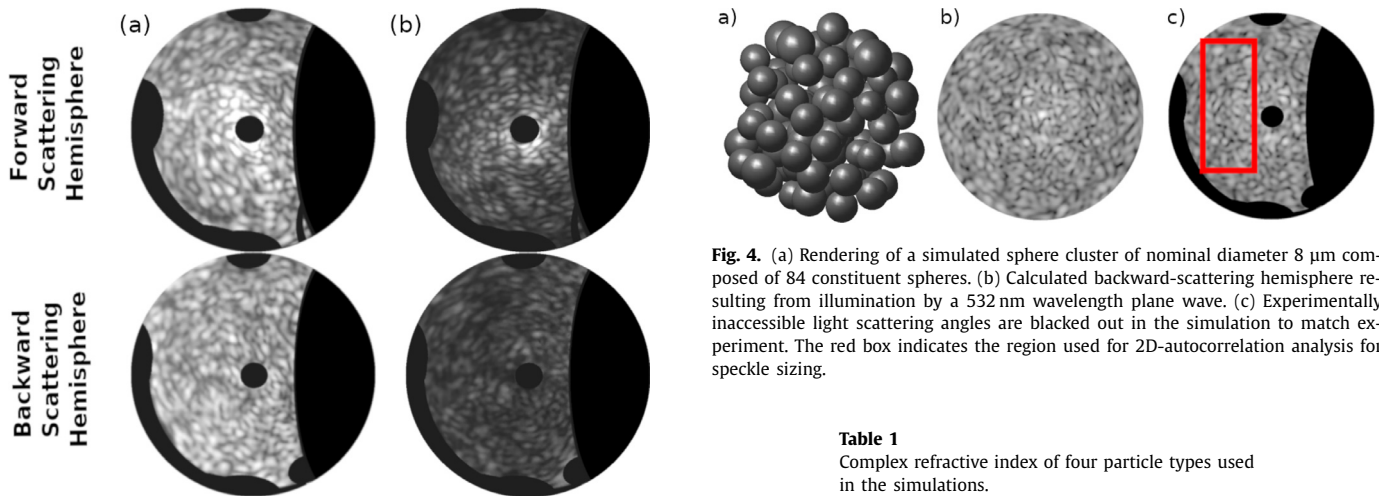


**Fig. 3.** Experimentally captured TAOS patterns from 2 atmospheric particles displayed using spherical coordinates. The composition of the particles is unknown. The integrated irradiance of the light detected in (a) is six times larger than the light detected in (b). Note the speckle size seen in the two patterns is similar. A logarithmic scale is used to display the brightness.

collected TAOS patterns from atmospheric aerosols in Las Cruces, NM [9]. By performing simulations that mimic the TAOS patterns captured by this instrument, we intend to explore this hypothesis and gain insight into how TAOS patterns can provide information about single-particle absorption.

### 3. Simulation and speckle analysis

Simulated TAOS patterns were calculated using Mackowski's publicly available MSTM Fortran code that calculates electromagnetic scattering and absorption properties of multiple sphere clusters [19,29]. A position file containing the location and radius of each constituent sphere in the cluster is generated prior to running the MSTM code. The position file is generated by filling a sphere, set to the diameter of the cluster, with randomly generated points. These points represent the locations of the centers of the initial constituent spheres. Next, using the minimum diameter set for the constituent spheres, spheres are removed to prevent any overlap in volume. Finally, once all overlapping spheres have been removed, the radius of each constituent sphere is increased until it is about to touch the surface of another constituent sphere. This process results in a fairly tightly-packed sphere-like cluster with a very small distribution of constituent sphere diameters, as shown in Fig. 4(a). The polydispersity of the constituent spheres is approximately 6

The incident wavelength for the MSTM simulation was set to be 532 nm circularly polarized plane waves to match experimen-

**Fig. 4.** (a) Rendering of a simulated sphere cluster of nominal diameter 8  $\mu\text{m}$  composed of 84 constituent spheres. (b) Calculated backward-scattering hemisphere resulting from illumination by a 532 nm wavelength plane wave. (c) Experimentally inaccessible light scattering angles are blacked out in the simulation to match experiment. The red box indicates the region used for 2D-autocorrelation analysis for speckle sizing.

**Table 1**

Complex refractive index of four particle types used in the simulations.

Particle type	Complex refractive index
Oceanic	$1.38 + i 4.3 \times 10^{-9}$
Sulfate	$1.53 + i 7 \times 10^{-3}$
Dust	$1.53 + i 8 \times 10^{-3}$
Soot	$1.75 + i 0.43$

tal conditions [9]. The value of the refractive index of the sphere clusters was varied to match four different particle types: oceanic, sulfate, dust, and soot [30–32]. These particle types provide a good range of values to test our technique and are physically relevant to aerosol optics. Table 1 displays the real and imaginary components of the refractive index for these four particle types. Using the MSTM code, the forward- and backward-scattering hemispheres are calculated for each simulated cluster. The backward-scattering hemisphere for the particle shown in Fig. 4(a) is displayed in Fig. 4(b). Finally, to mimic the experimental geometry, scattering angles that are inaccessible in the TAOS instrument are blacked out, as shown in Fig. 4(c).

As discussed in Section 2, the size of the particle can be estimated from the speckle in the TAOS patterns. The following procedure was used to determine the nominal size of the speckle from the simulated scattering patterns. Once the forward- and backward-scattering hemispheres were determined, the logarithm of the irradiance is calculated. Given the large dynamic range of elastic light scattering, using the logarithm of the irradiance improves analysis of the speckle features. The 2D-autocorrelation function of a subregion of the backward-scattering hemisphere is then calculated using MATLAB (The Mathworks Inc.) to determine the nominal speckle size. This subregion is indicated by a red rectangle in Fig. 4(c) and was chosen to both maximize the size of the region analyzed as well as avoid any scattering angles that are

inaccessible to the experimental apparatus. The uniformity of the speckle in Fig. 4(b) suggests that the results of this paper are not sensitive to the selection of subregion as long as a large subregion is selected to ensure good statistics. That said, the near-forward scattering angles should be avoided since those are heavily influenced by diffraction. Using the Image Processing Toolbox for MATLAB, the 2D-autocorrelation function is calculated and binarized with a threshold of 50% of the peak value. By performing the binarization, the central peak takes on a shape similar to an ellipse. Using the MATLAB *regionprops* function, the length (in pixels) of the major axis of the ellipse is determined. This value was then converted into an angular extent using the known conversion from pixels to degrees. This value, labeled  $\Delta\theta$ , serves as a measure of the nominal width of the speckle.

#### 4. Results

A series of calculations were performed using the MSTM code to explore how speckle width and integrated irradiance varied with cluster properties such as the real and imaginary parts of the refractive index, the cluster diameter, the size of the constituent spheres of the cluster, as well as different configurations of a cluster. The starting point for the analysis was a cluster diameter of  $6\ \mu\text{m}$  with constituent spheres of minimum diameter of  $0.791\ \mu\text{m}$  and complex refractive index  $1.53 + i\ 8 \times 10^{-3}$ . The speckle width and integrated irradiance were calculated as each parameter was individually varied while keeping all other parameters constant.

Fig. 5(a) shows how the integrated irradiance and speckle width change for 10 different configurations of the constituent spheres. For each configuration, the position of the constituent spheres is different while the cluster diameter, the minimum constituent sphere size, and complex refractive index are held constant. The effect of varying the configuration of the constituent spheres has minimal impact on the integrated irradiance and speckle width. Both quantities appear to be fairly independent of constituent sphere configuration.

Next, the constituent sphere minimal diameter is varied from  $0.34\ \mu\text{m}$  to  $2\ \mu\text{m}$  while keeping all other parameters constant. The integrated irradiance decreases, although not drastically, as shown in Fig. 5(b). The speckle width has limited variation. A similar procedure was followed to explore how the integrated irradiance and speckle width depend upon the real part of the refractive index. Again all cluster properties were kept constant except for the real part of the refractive index, which was varied from 1.3 to 2.0. The results, shown in Fig. 5(c), are similar in magnitude as when the constituent sphere size is changed.

The imaginary part of the refractive index ( $k$ ) is varied from  $10^{-8}$  to 1 while keeping all other parameters constant. The results, displayed in Fig. 5(d), show the speckle width remains fairly constant; whereas, integrated irradiance decreases by a factor of 7. Thus the length scales are in good agreement and the decrease in the integrated irradiance primarily occurs between  $k = 0.002$  and  $k = 0.04$ , which corresponds to a penetration depth of the light of  $21\ \mu\text{m}$  and  $1\ \mu\text{m}$ , respectively. The cluster diameter is  $6\ \mu\text{m}$  for this simulation. Thus the decrease in integrated irradiance is occurring when a significant fraction of the light is being absorbed when traversing the particle.

Finally, the cluster diameter is varied from  $1\ \mu\text{m}$  to  $10\ \mu\text{m}$  while keeping all other parameters constant except for the minimum constituent sphere diameter. In particular, to vary the cluster diameter, the entire cluster was scaled in size and, therefore, the constituent spheres were also scaled by the same factor. The results are shown in Fig. 5(e). As expected, both the integrated irradiance and the speckle width vary greatly. The speckle width dramatically decreases from  $20^\circ$  to  $4^\circ$  over this change in cluster size while the integrated irradiance increases by more than a factor of 30.

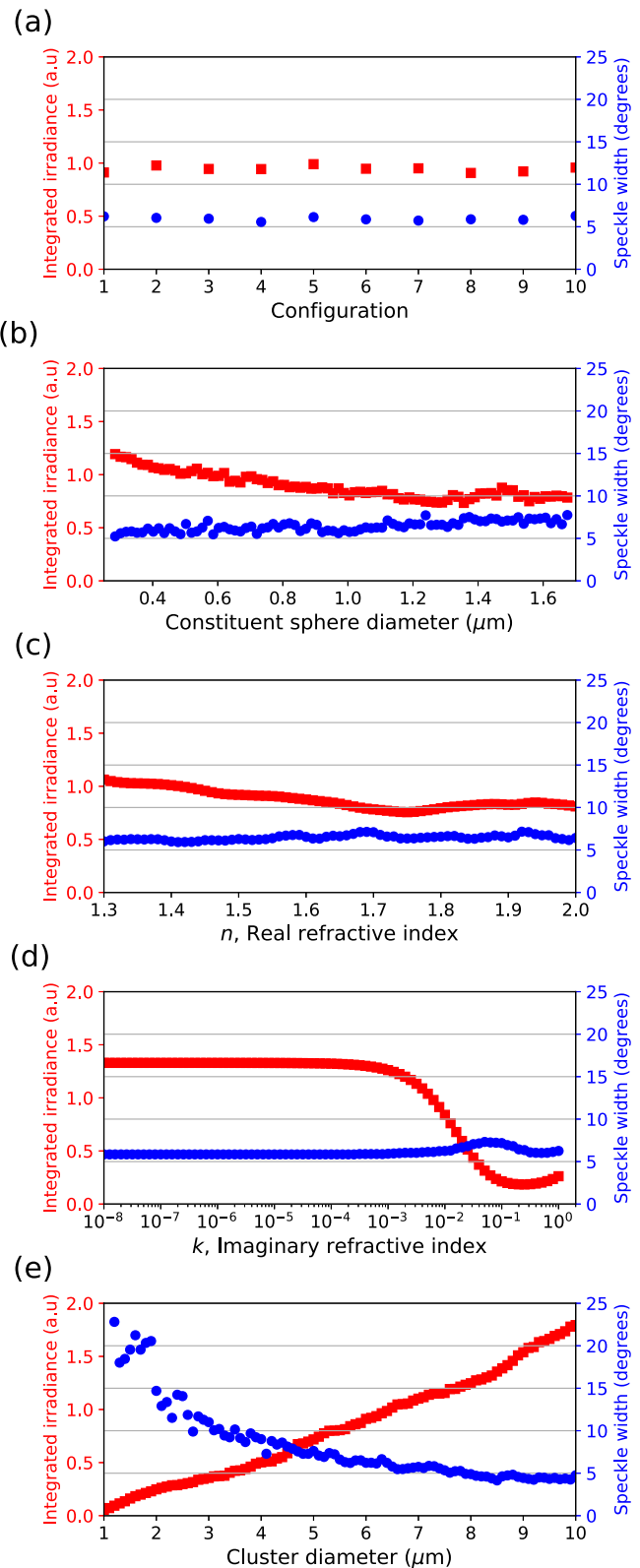
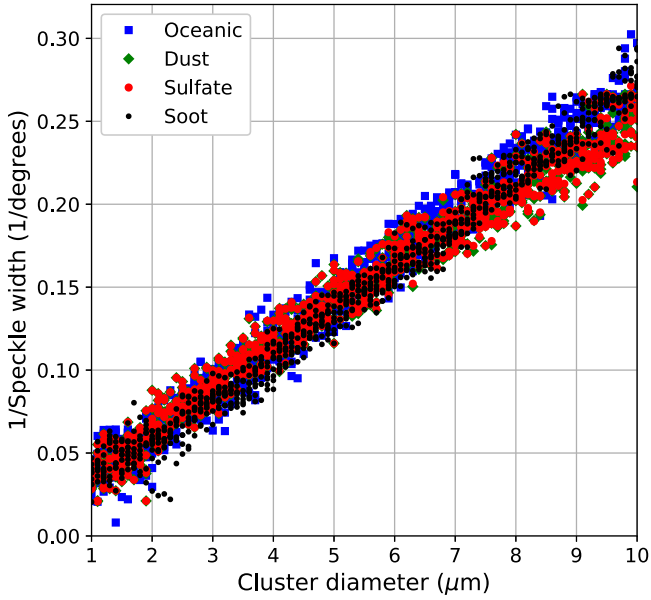


Fig. 5. The speckle width and integrated irradiance were calculated as each parameter of a cluster was individually varied while keeping all other parameters constant. The starting point for the analysis was a cluster with a nominal diameter of  $6\ \mu\text{m}$  with constituent spheres of minimal diameter of  $0.791\ \mu\text{m}$  and complex refractive index  $1.53 + i\ 8 \times 10^{-3}$ . (a) The position of the constituent spheres is varied. (b) The minimal diameter of the constituent spheres is varied. (c) The real part of the refractive index is varied. (d) The imaginary part of the refractive index is varied. (e) The diameter of the cluster is varied.



**Fig. 6.** Relationship between particle cluster diameter and average speckle width. Results appear to be largely independent of particle composition.

From these results, we conclude the speckle width is independent or weakly dependent on all cluster properties except cluster diameter suggesting speckle width could be an excellent measure of cluster size. This agrees well with the work of other groups [23,26,27]. We believe the basis for this result is primarily geometrical. In particular, the appearance of speckle is an interference phenomenon which derives from the difference in phase of interacting light waves. This difference in phase is being driven by path length differences from different parts of the particle to the far field point being detected. When the size of the particle is increased, so is the path length differences, which results in smaller speckle. A good analogy is the spacing of the slits in a two-slit interference experiment. As the slit spacing increases, the angular frequency of the interference pattern increases resulting in smaller interference fringes. In our simulation, as the particle size increases, the speckle gets smaller.

Next, we explore whether we can differentiate between different particle types of aerosol particles, like oceanic sea-salt, sulfate, dust, and soot aerosols of different cluster sizes using the two experimentally accessible parameters of speckle width and integrated irradiance. Ideally, the speckle width solely depends upon the size of a cluster and no other particle properties. To check this, forward- and backward-scattering hemispheres are calculated using the MSTM code for various size clusters from 1  $\mu\text{m}$  to 10  $\mu\text{m}$  as well as 10 different configurations for each cluster. The complex refractive index of the constituent spheres is set to values given in Table 1. A total of 3640 simulated TAOS patterns are calculated. The inverse of the speckle width is plotted as a function of cluster diameter. As shown in Fig. 6, the relationship appears to be linear, although the dynamic range is quite small. The correlation coefficient between the inverse of the speckle width and the cluster diameter is 0.98. All four particle types collapse onto a single curve indicating that indeed speckle width is primarily a function of cluster size, with only a minimal dependence on aerosol type. In performing a linear fit to the data, the relationship between speckle width in degrees ( $\Delta\theta$ ) and the cluster diameter in micrometers ( $D_{\text{cluster}}$ ) is captured by the expression

$$\Delta\theta = 37.0/D_{\text{cluster}}. \quad (1)$$

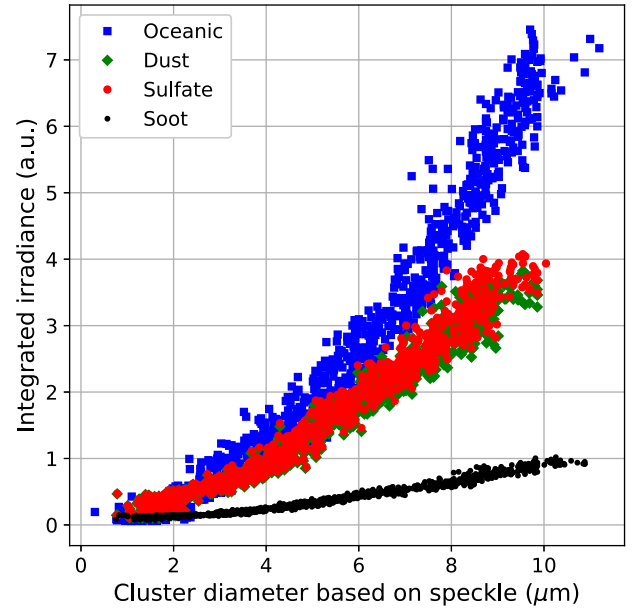


**Fig. 7.** Graph of two experimentally accessible variables: Cluster diameter determined from the speckle width and the integrated irradiance of the scattering pattern. Highly absorbing clusters are clearly distinguishable from other clusters.

The simulated TAOS data used to create Fig. 6 are further analyzed to explore whether the scattering patterns from different aerosol types, i.e. oceanic, dust, sulfate, and soot, can be distinguished from each other. In particular, for each simulated TAOS pattern, the cluster diameter is estimated from the speckle width and the integrated irradiance is calculated. By plotting these two quantities for all 3640 simulated TAOS patterns, the different particle types separate as shown in Fig. 7. Highly absorbing soot particles have a much lower integrated irradiance than oceanic, dust, or sulfate particles of similar cluster size. Furthermore, non-absorbing oceanic particles have a slightly higher integrated irradiance than sulfate or dust particles. Sulfate and dust particles, which have very similar complex refractive indices, are essentially indistinguishable from each other. As an example, for a 10  $\mu\text{m}$  nominal diameter cluster, the integrated irradiance of a particle with optical properties similar to sulfate or dust is almost 4 times larger than a particle with optical properties similar to soot. The integrated irradiance of an oceanic particle is almost 7 times larger than that of soot. The separation between particle types diminishes as the cluster size is reduced. Below 6  $\mu\text{m}$  in diameter, sulfate and dust data points become indistinguishable from oceanic data points. Below 2  $\mu\text{m}$ , the data points for all four particles overlap. This result is not surprising if one considers that absorption should scale with particle volume, and thus elastic scattering from the smaller clusters should be more weakly dependent on the absorptive properties of the clusters.

Although Fig. 7 is promising and suggests that experimentally captured TAOS patterns could be used to distinguish between particles with different absorption properties, further studies are needed. For example, all the simulated TAOS patterns for this work were calculated from tightly-packed clusters of spheres. Thus, it is unclear how a change in particle morphology away from clusters of spheres would affect the analysis. However, Ulanowski et al. finds that speckle analysis is fairly robust in determining the size of particles of different origin and refractive index such as rough dust, smooth dust, a living cell, sphere clusters and a nearly smooth prismatic particle analogous to ice [23]. Clusters of spheres appear to depart somewhat from the general trend with a 30–40% reduction in speckle area.

Another challenge this approach faces is making absolute scattering intensity measurements by measuring the integrated irradiance of the detected TAOS pattern. Absolute intensity measurements are difficult and suffer from errors due to laser beam power and detector gain fluctuations, particle misalignment, and varying background levels. For example, the current instrument to capture TAOS patterns has fluctuations of integrated irradiance as large as a factor of 2 for monodispersed polystyrene spheres. This suggests that further modifications of the instrument are needed before detailed information can be gleaned from absolute scattering intensity measurements.

## 5. Summary

In this work, we present an approach for distinguishing between single non-spherical aerosol particles with varying absorptive properties in the coarse-mode size range. To test the approach, we simulated the TAOS patterns captured by a previously constructed instrument. Following the work of other groups, we found the speckle in the simulated TAOS patterns strongly correlates with the size of the aerosol particle, which is a tightly-packed cluster of spheres for our simulation. In particular, the nominal width of the speckle ( $\Delta\theta$ ) is related to the diameter of the cluster ( $D_{cluster}$ ) by the expression  $\Delta\theta = 37/D_{cluster}$ . In addition, we found that the integrated irradiance of the TAOS pattern to have a strong positive correlation with the size of the cluster and a negative correlation with the imaginary component of the refractive index of the constituent spheres in the cluster. With an independent measure of cluster size from the speckle, we show integrated irradiance can be used to distinguish between clusters that are strongly absorbing, weakly absorbing, and non-absorbing. This characterization becomes more difficult as the cluster size shrinks to below 2  $\mu\text{m}$ .

## Acknowledgments

This work was supported by the [US Army Research Office](#), grant no. [W911NF1420098](#). Thanks to Ronald G. Pinnick for collecting the TAOS images shown in [Fig. 3](#) and to Daniel Landgraf for fruitful conversations and assisting in the creation of [Fig. 2](#).

## Supplementary material

Supplementary material associated with this article can be found, in the online version, at doi:[10.1016/j.jqsrt.2018.12.005](https://doi.org/10.1016/j.jqsrt.2018.12.005).

## References

- [1] Bond TC, Doherty SJ, Fahey D, Forster P, Berntsen T, DeAngelo B, et al. Bounding the role of black carbon in the climate system: a scientific assessment. *J Geophys Res* 2013;118(11):5380–552.
- [2] Sokolik IN, Toon OB. Incorporation of mineralogical composition into models of the radiative properties of mineral aerosol from uv to ir wavelengths. *J Geophys Res* 1999;104(D8):9423–44.
- [3] Andreae M, Gelencsér A. Black carbon or brown carbon? the nature of light-absorbing carbonaceous aerosols. *Atmos Chem Phys* 2006;6(10):3131–48.
- [4] Moosmüller H, Chakrabarty R, Arnott W. Aerosol light absorption and its measurement: a review. *J Quant Spectrosc Radiat Transfer* 2009;110(11):844–78.
- [5] Samset BH, Stjern CW, Andrews E, Kahn RA, Myhre G, Schulz M, et al. Aerosol absorption: progress towards global and regional constraints. *Curr Clim Change Rep* 2018:1–19.
- [6] Von Klot S, Cyrus J, Hoek G, Kühnel B, Pitz M, Kuhn U, et al. Estimated personal soot exposure is associated with acute myocardial infarction onset in a case-crossover study. *Prog Cardiovasc Dis* 2011;53(5):361–8.
- [7] Weinhold B. Global bang for the buck: cutting black carbon and methane benefits both health and climate. *Environ Health Perspect* 2012;120(6):a245.
- [8] Mason BJ, King S-J, Miles RE, Manfred KM, Rickards AM, Kim J, et al. Comparison of the accuracy of aerosol refractive index measurements from single particle and ensemble techniques. *J Phys Chem A* 2012;116(33):8547–56.
- [9] Aptowicz KB, Pan Y-L, Martin SD, Fernandez E, Chang RK, Pinnick RG. Decomposition of atmospheric aerosol phase function by particle size and asphericity from measurements of single particle optical scattering patterns. *J Quant Spectrosc Radiat Transfer* 2013;131:13–23.
- [10] Willoughby RE, Cotterell MI, Lin H, Orr-Ewing AJ, Reid JP. Measurements of the imaginary component of the refractive index of weakly absorbing single aerosol particles. *J Phys Chem A* 2017;121(30):5700–10.
- [11] Nakagawa M, Nakayama T, Sasago H, Ueda S, Venables DS, Matsumi Y. Design and characterization of a novel single-particle polar nephelometer. *Aerosol Sci Technol* 2016;50(4):392–404.
- [12] Gong Z, Pan Y-L, Wang C. Characterization of single airborne particle extinction using the tunable optical trap-cavity ringdown spectroscopy (ot-crds) in the uv. *Opt Express* 2017;25(6):6732–45.
- [13] Oshima N, Kondo Y, Moteki N, Takegawa N, Koike M, Kita K, et al. Wet removal of black carbon in asian outflow: aerosol radiative forcing in east asia (a-force) aircraft campaign. *J Geophys Res* 2012;117(D3).
- [14] Allan JD, Morgan WT, Darbyshire E, Flynn MJ, Williams PI, Oram DE, et al. Airborne observations of iepox-derived isoprene soa in the amazon during sambba. *Atmos Chem Phys* 2014;14(20):11393–407.
- [15] Stephens M, Turner N, Sandberg J. Particle identification by laser-induced incandescence in a solid-state laser cavity. *Appl Opt* 2003;42(19):3726–36.
- [16] Schwarz J, Gao R, Fahey D, Thomson D, Watts L, Wilson J, et al. Single-particle measurements of midlatitude black carbon and light-scattering aerosols from the boundary layer to the lower stratosphere. *J Geophys Res* 2006;111(D16).
- [17] Moteki N, Kondo Y. Effects of mixing state on black carbon measurements by laser-induced incandescence. *Aerosol Sci Technol* 2007;41(4):398–417.
- [18] Moteki N, Kondo Y, Nakamura S-i. Method to measure refractive indices of small nonspherical particles: application to black carbon particles. *J Aerosol Sci* 2010;41(5):513–21.
- [19] Mackowski DW, Mishchenko MI. Calculation of the t matrix and the scattering matrix for ensembles of spheres. *JOSA A* 1996;13(11):2266–78.
- [20] Aptowicz KB, Pan Y-L, Chang RK, Pinnick RG, Hill SC, Tober RL, et al. Two-dimensional angular optical scattering patterns of microdroplets in the mid infrared with strong and weak absorption. *Opt Lett* 2004;29(17):1965–7.
- [21] Holler S, Pan Y-L, Chang RK, Bottiger JR, Hill SC, Hillis DB. Two-dimensional angular optical scattering for the characterization of airborne microparticles. *Opt Lett* 1998;23(18):1489–91.
- [22] Holler S, Zomer S, Crosta GF, Pan Y-L, Chang RK, Bottiger JR. Multivariate analysis and classification of two-dimensional angular optical scattering patterns from aggregates. *Appl Opt* 2004;43(33):6198–206.
- [23] Ulanowski Z, Hirst E, Kaye PH, Greenaway R. Retrieving the size of particles with rough and complex surfaces from two-dimensional scattering patterns. *J Quant Spectrosc Radiat Transfer* 2012;113(18):2457–64.
- [24] Ulanowski Z, Kaye PH, Hirst E, Greenaway R, Cotton RJ, Hesse E, et al. Incidence of rough and irregular atmospheric ice particles from small ice detector 3 measurements. *Atmos Chem Phys* 2014;14(3):1649–62.
- [25] Fu R, Wang C, Muñoz O, Videen G, Santarpia JL, Pan Y-L. Elastic back-scattering patterns via particle surface roughness and orientation from single trapped airborne aerosol particles. *J Quant Spectrosc Radiat Transfer* 2017;187:224–31.
- [26] Brunel M, Shen H, Coëtmelec S, Gréhan G, Delobel T. Determination of the size of irregular particles using interferometric out-of-focus imaging. *Int J Opt* 2014;2014.
- [27] Talbi M, Gréhan G, Brunel M. Interferometric particle imaging of ice particles using a multi-view optical system. *Appl Opt* 2018;57(21):6188–97.
- [28] Fernandes GE, Pan Y-L, Chang RK, Aptowicz K, Pinnick RG. Simultaneous forward-and backward-hemisphere elastic-light-scattering patterns of respirable-size aerosols. *Opt Lett* 2006;31(20):3034–6.
- [29] Mackowski D, Mishchenko M. A multiple sphere t-matrix fortran code for use on parallel computer clusters. *J Quant Spectrosc Radiat Transfer* 2011;112(13):2182–92.
- [30] Box MA, Box GP. *Physics of Radiation and Climate*. CRC Press; 2015.
- [31] Kokhanovsky AA. *Aerosol Optics: Light Absorption and Scattering by Particles in the Atmosphere*. Springer Science & Business Media; 2008.
- [32] Levoni C, Cervino M, Guzzi R, Torricella F. Atmospheric aerosol optical properties: a database of radiative characteristics for different components and classes. *Appl Opt* 1997;36(30):8031–41.